

## DosiVox: Implementing Geant 4-based software for dosimetry simulations relevant to luminescence and ESR dating techniques

Loïc Martin,<sup>1\*</sup> Sébastien Incerti,<sup>2,3</sup> Norbert Mercier<sup>1</sup>

<sup>1</sup>Institut de Recherche sur les Archéomatériaux, UMR 5060 CNRS Université Bordeaux Montaigne, Centre de Recherche en Physique Appliquée à l'Archéologie (CRP2A), Maison de l'archéologie, 33607 Pessac Cedex, France

<sup>2</sup>CNRS, IN2P3, CENBG, UMR 5797, 33170 Gradignan, France

<sup>3</sup>Université de Bordeaux, CENBG, UMR 5797, 33170 Gradignan, France

\*Corresponding Author: loic.martin@u-bordeaux-montaigne.fr

Received: June 25, 2014; in final form: December 12, 2014

### Abstract

A C++ code, named *DosiVox* and based on the *Geant4* Monte Carlo simulation toolkit, was developed in order to provide a reliable and flexible tool for modeling a large variety of situations of interest in paleodosimetric dating techniques, and for simulating interactions of usual particles ( $\alpha$ ,  $\beta$  and  $\gamma$ ) through complex geometries. *DosiVox* allows the user to define a three dimensional grid, in the simulation space whose voxel dimensions, materials and radioactive contents (U, Th, K) are set by a user-friendly graphical interface. No skills in C++ programming are required. Some of the possibilities offered by *DosiVox* are presented here through a series of examples.

**Keywords:** Dosimetry, Dating, Luminescence, ESR, Simulation, Sediment

### 1. Introduction

Almost thirty years ago, Aitken (1985) summarised the basis of the thermoluminescence dating technique, outlining important information relevant to the dosimetry of the samples to be dated, and also the basis for delivering known doses to samples using artificial radioactive sources, and for determining the natural dose rates to which this sample has been exposed. In particular, he collected a series of dosimetric calculations (performed by several authors) which are still of primary importance today in any dating application as, for instance, those related to  $\beta$ - and  $\gamma$ -dose gradients (Aitken

et al., 1985) or to attenuation factors of the dose rates (Zimmerman, 1971; Mejdahl, 1979; Bell, 1980).

This author also exposed a technique from Fleming (1970) – the inclusion technique used for pottery dating – which, from a dosimetric point of view, can be seen as an ideal case: the grains which are the sources of the luminescence signal, are considered as embedded in a homogeneous matrix containing a uniform distribution of radioelements. In that case, the density of grains in the material (i.e. the number of grains per unit of volume) is supposed to be low enough to ensure that the presence of these grains does not alter the homogeneity of the matrix and the distribution of the radioelements, and has no influence on the particles fluxes induced by the decay of these radioelements (Guérin et al., 2012). Although defined for pottery dating, this technique is nowadays largely applied to sediment dating and it is questionable whether this model is sufficient to deal with dose rate calculations for the more complex situations which may arise.

Beyond sediment dating, the luminescence or ESR techniques are also used for dating a large diversity of samples (burnt stones, teeth, ...), each one being characterized by its elemental chemical composition, its geometry and its radioactive elements distribution. Moreover, in most cases, the distributions of the radioactive isotopes in the sample itself and its environment - from distances ranging from a few microns up to tenths of centimeters are heterogeneous, making precise dosimetric descriptions difficult, and often leading to adoption of simplifying hypotheses in order to manage the system.

Clearly dosimetry remains at the heart of the dating process, being critical to calibration of artificial sources used for irradiation in the laboratory, and for calculation of any

dose rate. In order to assess the various dosimetric hypotheses usually needed to calculate ages, we have developed a flexible dosimetric tool named *DosiVox*, which is based on the general purpose *Geant4* Monte Carlo toolkit developed at CERN for simulating particle-matter interactions (Agostinelli et al., 2003; Allison et al., 2006). Our objective was to prepare a tool which can be used to model both simple and complex cases (as those described above) and to perform dose-rate calculations. Technically, this software allows the user to create a model of the sample and its environment using a graphical interface which generates a pilot text file. No skills in programming or in the usage of the *Geant4* libraries are then required. In this paper, we outline the program operation and illustrate some of its possibilities for dose rate evaluation in simple and more complex cases.

## 2. Program description

The *Geant4* toolkit is a set of C++ public libraries which can be compiled with C++ codes to simulate particle-matter interactions by Monte Carlo methods. *Geant4* incorporates a wide range of physics models applied to diverse situations, ranging from high energy physics to medical and space applications (<http://www.Geant4.org>) and can be used to simulate interactions in complex detectors. In dosimetric applications relevant to dating techniques, *Geant4* has already been used for dose calculations (Guérin et al., 2012), but up to now, its potential had been under-exploited. The *DosiVox* program aims to provide a reliable and flexible tool for modeling a large variety of situations of interest in paleodosimetric dating techniques, and simulating interactions of ionizing radiation ( $\alpha$ ,  $\beta$  and  $\gamma$ ) in complex geometries. The code developed has been compiled with *Geant* version 4.10p01, and uses the electromagnetic physics list provided by the G4PenelopePhysics constructor (Ivanchenko et al., 2011), which is based on the 2008 version of the PENLOPE Monte Carlo code (Baró et al., 1995) and adapted to the transport of low energy particles (Sempau et al., 2003). The secondary particle production cut can be set by the user, in order to match the desired simulations conditions. No step limit was imposed.

*DosiVox* allows the user to define a “World” volume for simulation in a three dimensional grid (e.g., Fig 1), whose voxel dimensions, material and radioactive contents (U, Th, K) are set through a graphical user interface. This geometrical grid is implemented by successively dividing the volume along the three axes and implementing a nested parametrization of the resulting voxels. This method considerably reduces the time and memory required for geometry optimization and navigation during simulations (Aso et al., 2007; Incerti et al., 2009). Grids with 1 to 300 million voxels, can be loaded in *DosiVox* as 3D images, which decreases the memory requirements for geometry optimization by a factor of about 20 compared to standard parametrization methods.

Different detectors, which are defined in ‘parallel worlds’, can be superimposed on this grid: a vertical cylindrical probe segmented in different parts, a random packing of

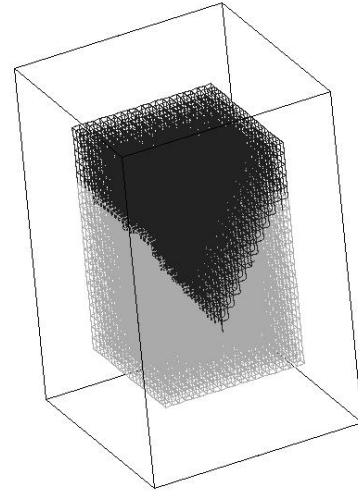


Figure 1. Main voxels grid image. The different tints indicate the different materials in the voxels.

spheres (modeling the grains) in a rectangular prism, or a sub-voxelised voxel.

The first of these detectors, the cylindrical probe, is always present in all the simulations but does not interact with the particles or the materials. It only records both the energies of the primary emitted particles and the energy deposited in each of its segments during the whole simulation, and accumulates them. The absorbed dose, as being defined as the deposited energy divided by the density of the material present in the center of this volume, multiplied by the volume of the probe segment itself (defined by the user), is also calculated. Calculation of the absorbed dose relatively to the infinite matrix dose is then performed using these data. The other detector types are sensitive to all particles and record the energy and hence, the dose deposited. At maximum, only one type of these detectors can be defined during a simulation.

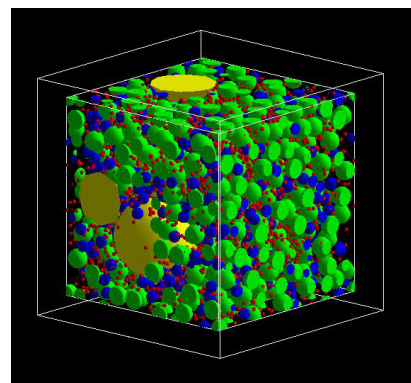


Figure 2. Random packing of grains in a defined box. The edge effects are corrected by a boundary recurrence.

The random packing of spheres was created in order to represent grains in a sedimentary medium; it is defined inside a box whose maximum dimensions are equal to those of one

voxel, and takes into account the material of the grains, their granulometry and their state of compaction (Fig. 2). This detector can also be replicated along the vertical axis of the simulation space - filling up the full height of the geometry with successive boxes containing grains packed to correspond to the material of each intercepted voxel. Moreover, the user can choose to emit particles from the spheres (i.e. the grains) or from the surrounding matrix filling these boxes. The dose deposited in each individual grain is then recorded during the simulation and is available in the results files.

The last detector is a sub-voxelised voxel allowing to define objects with a potentially higher resolution than the main grid, and to register the dose emitted and deposited in all parts of this virtual detector. The voxel chosen by the user is divided into a 3D voxel grid, and as with the main grid, the user can assign the material of choice and its radioactivity content to each of these sub-voxels. The interface allows a  $20 \times 20 \times 20$  voxel grid to be defined with its material properties and radioactive contents. Voxelised 3D grey-scale images can also be used to define the detector as well as the use of files resulting from imaging methods (image processing may be necessary to transform images in vertex to image in voxel, which is required for *DosiVox*): in both cases, high resolutions can then be obtained. In the software, the dose deposited in each voxel of this detector, and the dose emitted from it, are recorded. The results are given in two ways: a summary of the dose for each material constituting the detector, and a succession of 3D map slices in ASCII matrix format allowing representation of the deposited dose in 3D, either for all the sub-voxels of the detector, or only for the sub-voxels filled with a particular material. The values in the ASCII files represent 16 bit resolution grey scale levels, and are proportional to the dose deposited.

In many cases of simulation, it is convenient to normalize the dose absorbed in the detectors by the total energy emitted by unit of mass (corresponding to the infinite matrix dose in the case of an infinite medium). The dose rates in the detectors can be then obtained by multiplying this ratio by the infinite matrix dose rate tabulated for the radioelement contents in the corresponding material. As a consequence, the simulation results normalized in this way are equivalent to dose rates.

### 3. Examples of simulations using *DosiVox*

The following section gives examples illustrating some of the possibilities of the *DosiVox* software. Simulations of  $\gamma$ -,  $\beta$ - and  $\alpha$ -particles have been carried out for spectra of the U- and Th-series,  $^{40}\text{K}$  and  $^{137}\text{Cs}$ . The radioactive decay chains, if applicable, were treated as being in secular equilibrium. However, it is worth noting that, since the emission spectra are accessible to the user (and are defined as text files), modifications of this assumption could easily be implemented.

For visualisation of 2D and 3D images, an open sources image analysis and processing software was used: *ImageJ* (Abràmoff et al., 2004; Rasband, 1997–2012; Schneider et al., 2012), available at the website <http://imagej.nih.gov/ij/index.html>.

*ImageJ* was also used to create parts of models presented in this paper, as mentioned in the corresponding paragraphs.

#### 3.1. $\gamma$ -dose attenuation by a limestone wall

The first example considered here is a sediment deposit placed alongside a limestone block. This is similar to that discussed by Aitken in Appendix H of his 1985 book. Limestones are usually considered less radioactive than clay-rich sediments, and an attenuation of the  $\gamma$ -dose rate (compared to the infinite matrix dose in the sediment) is then expected in the first tens of centimeters from the limestone surface.

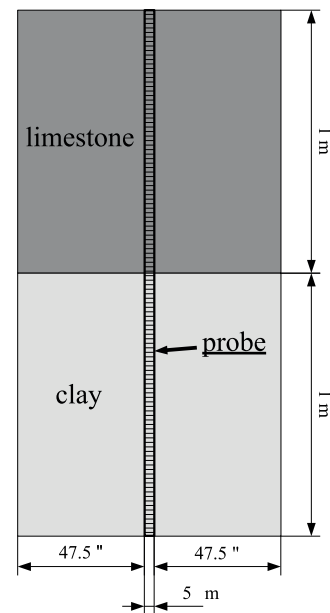


Figure 3. Plan of the geometry of the limestone wall model

To model this configuration, a limestone block has been designed in the graphical interface, by simply filling the first ten levels of voxels in the Z axis with a limestone material (chemical composition: 70 % (in mass)  $\text{CaCO}_3$ , 30 %  $\text{MgCO}_3$ , density  $2.7 \text{ g/cm}^3$ , water content: 10 % by weight) using an automated function available in the interface. The last ten levels were filled with a clay material representing the sediment (chemical composition: 55 %  $\text{SiO}_2$ , 35 %  $\text{Al}_2\text{O}_3$ , 10 %  $\text{Fe}_2\text{O}_3$ , density  $2.0 \text{ g/cm}^3$ , water content: 15 % by weight). The probe detector was positioned vertically in the middle of the simulation space, perpendicular to the boundary between the limestone and the clay (see Fig. 3)  $\gamma$ -photons from  $^{40}\text{K}$  were generated, assuming a concentration in limestone ten times lower than in clay. The dose distribution absorbed by the local material in the probe shown in Fig. 4 is normalised by the infinite matrix dose delivered in the clay sediment, which is simply obtained from the sum of the energies of the primary particles emitted in the clay per unit of mass. In this simulation, the average of the energy per mass emitted from the probe segment containing the clay material has been used to calculate the infinite matrix dose.

As expected the decrease of dose at the boundary between

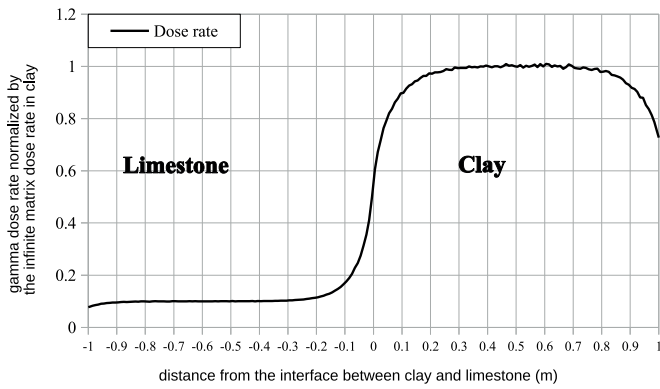


Figure 4.  $\gamma$ -dose rate profile of the simulation of a limestone wall adjoining a clay sediment

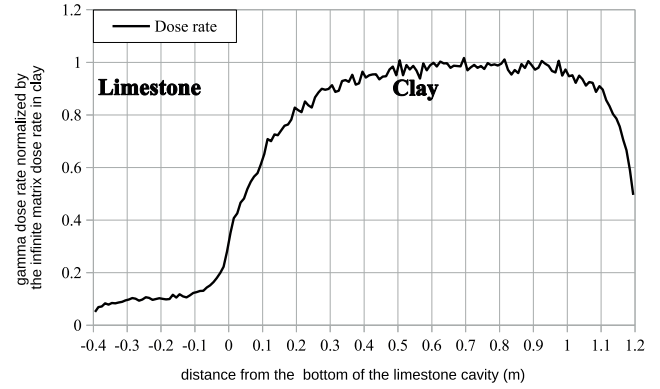


Figure 6.  $\gamma$ -dose rate profile of the simulation of a limestone cavity filled by a clay sediment

the limestone and the clay can be clearly observed. Dose attenuation can also be seen at the extremities of the graphic as a result of edge effects in the simulation, corresponding to the limits on the Z axis of the model grid. The continuity of the model is broken at these points, because of the non-radioactive void surrounding the voxelised grid.

A more complex configuration has been considered in the next example in which the sediment fills a limestone cavity. The cavity geometry, also created with the graphical interface, is represented in Fig. 5, and the probe remaining in the middle of the model as indicated in the figure. The same radioactive contents have been defined for the materials as for the precedent simulation, and the  $\gamma$ -dose profile calculated and normalized to the infinite matrix dose in the clay is shown in Fig. 6. As expected, the dose rate variations clearly differ from that of the previous configuration. As in the preceding model, edge effects can be observed at the graphic edges. The present example can easily be modified to reproduce complex boundaries between two or more media with different properties and radioactive contents.

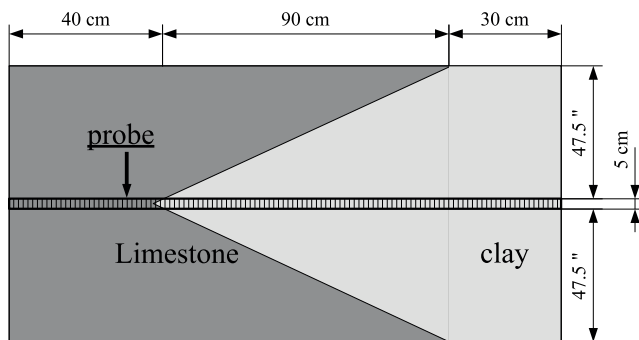


Figure 5. Plan of the geometry of the limestone cavity model

### 3.2. $\gamma$ -irradiation of a dosimeter for source calibration

In most dating applications, the dose accumulated by a sample is determined by comparing the natural signal with the one induced by an artificial  $\beta$ -source, hence the impor-

tance to get an accurate calibration of this source. One way to calibrate it is to irradiate a phosphor contained in a tube (hereafter called a dosimeter) with a calibrated  $\gamma$ -ray beam, and to compare the induced signals with those generated by the  $\beta$ -source. Here, we consider a dosimeter composed of a duralumin tube filled with a powder of quartz grains, and closed with a nylon screw (Fig. 7).

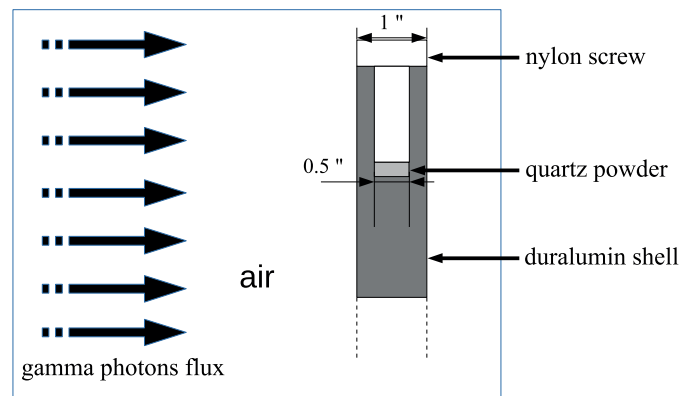


Figure 7. Plan of the geometry of the dosimeter irradiation model

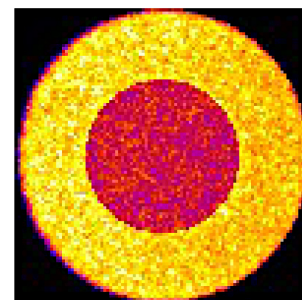


Figure 8. Map of the dose distribution in the quartz powder and its duralumin shell from an artificial irradiation (arbitrary scale)

This configuration was modeled using a 3D image of the dosimeter as input for the voxelised detector. This image has been created with *ImageJ*, and saved as an 8 bits text im-

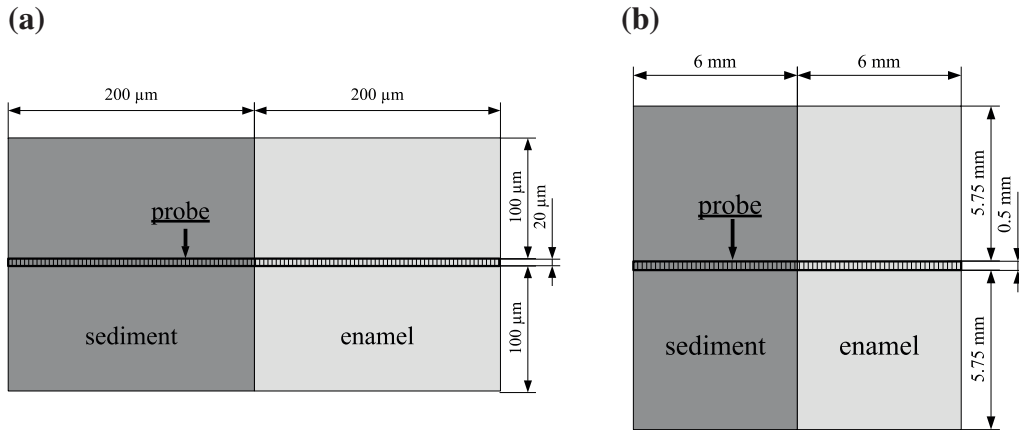


Figure 9. Plan of the geometry of enamel adjoining a sediment: (a) plan for the  $\alpha$ -particles simulation, (b) plan for the  $\beta$ -particles simulation

age sequence (in ASCII format), where each grey level represents a material constituting the dosimeter. A radioactive zone has been defined in the main voxel grid with the interface, and an unidirectional emission of  $\gamma$ -particles with energy of 661.7 keV (corresponding to the  $\gamma$ -emission of  $^{137}\text{Cs}$ ) has been chosen. For this purpose, the text file defining the emission spectrum has been modified. The voxelised detector, carrying the dosimeter geometry and the materials, has been positioned in the  $\gamma$ -flux (Fig. 7). The map of the absorbed dose in a slice of the dosimeter at the level of the phosphor is shown in Fig. 8. This image corresponds to the ASCII result file obtained for this level of the detector, and read by *ImageJ* as an image.

In this figure one can notice a nearly homogeneous dose distribution inside the quartz grains, even though a crescent form area of low dose in the left part of the duralumin tube is observable. At last, this kind of simulations allows calculating the fraction of energy absorbed in the tube and conse-

quently, improves the determination of the dose absorbed by the phosphor used for the  $\beta$ -source calibration.

### 3.3. $\beta$ - and $\alpha$ -dose attenuation factors in enamel

ESR dating of teeth requires the determination of the dose rates received by the enamel, which is the dated material. Enamel is generally considered to be a low-radioactive material, and it receives its dose mainly from the internal parts of the tooth and from the burial sediment. The attenuation of both  $\alpha$ - and  $\beta$ -particles, whose ranges are much lower than, or respectively, about the same size as the enamel thickness, have to be calculated for determining the correct dose rates. Simulations can provide these factors by modeling the enamel and the adjacent internal parts of the tooth and the sediment. This modeling was done directly with the pilot text file, creating two adjacent voxels instead of using the larger main grid. The first voxel was defined as a clay type sediment (chemical composition in mass:  $\text{SiO}_2$  55 %,  $\text{Al}_2\text{O}_3$  25 %,  $\text{Fe}_2\text{O}_3$  10 %,  $\text{CaO}$  5 %,  $\text{MgO}$  3 %,  $\text{K}_2\text{O}$  2 %,  $\text{Na}_2\text{O}$  1 %,  $\text{H}_2\text{O}$  1 %).

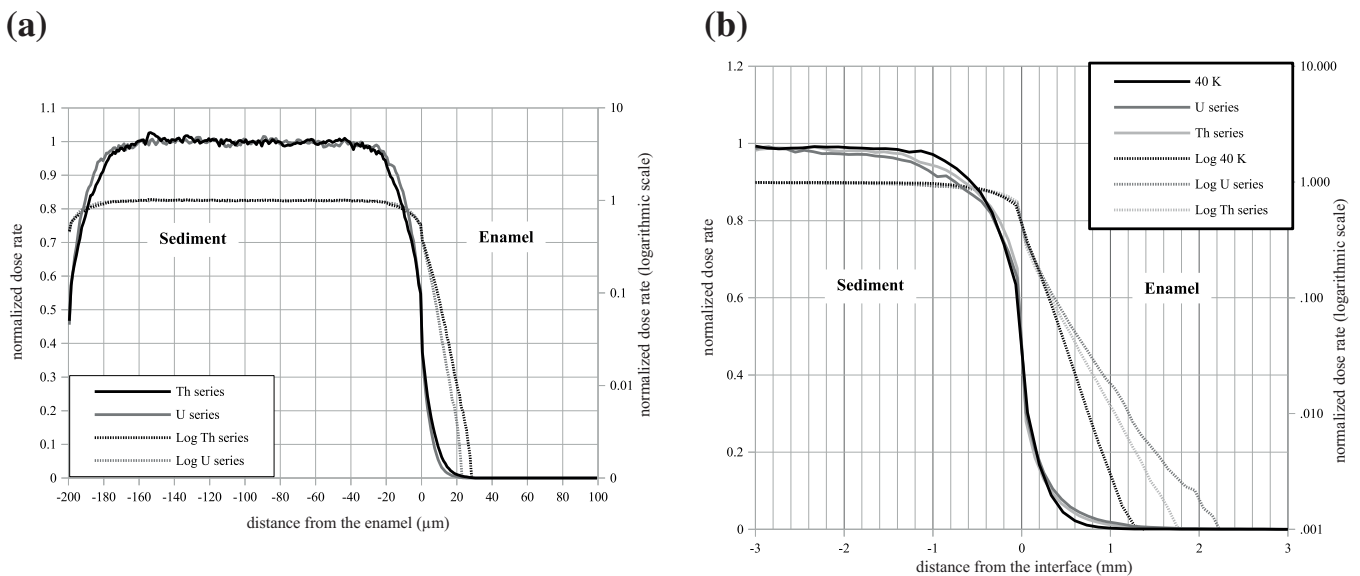


Figure 10. Dose rate attenuation in enamel from a clay sediment: (a)  $\alpha$ -dose attenuation, (b)  $\beta$ -dose attenuation

$\text{Al}_2\text{O}_3$  35 %,  $\text{Fe}_2\text{O}_3$  10 %; density:  $2 \text{ g/cm}^3$ , water content: 13 %), and the second is filled with hydroxyapatite (chemical raw formula:  $\text{Ca}_5\text{P}_3\text{O}_{13}\text{H}$ ; density:  $3.8 \text{ g/cm}^3$ ), which is the main component of enamel. The vertical probe was positioned in the center of the simulation space, perpendicular to the boundary between the two voxels.  $\alpha$ - or  $\beta$ -particles were emitted from the sediment. In each situation, the voxel size was chosen to contain the entire radioactive environment that can be seen by the probe parts, superimposed on the enamel (Fig. 9). The absorbed  $\alpha$ - and  $\beta$ -dose profiles for the uranium and thorium series spectra (and  $\beta$  only for  $^{40}\text{K}$ ) are given in Fig. 10. For a better legibility, the  $\beta$ -dose profile has been restricted to the 6 central millimeters around the interface between sediment and enamel, and the 100 last micrometers of the  $\alpha$ -dose profile, where no dose deposition was recorded, are not shown.

The  $\alpha$ -dose attenuation profiles indicate that the range of these particles in the enamel is lower than  $30 \mu\text{m}$ . The  $\beta$ -particles range in enamel is close to 2 mm, and the  $\beta$ -dose profiles allow calculating the attenuation of the sediment dose rate.

### 3.4. $\beta$ -dosimetry in a Neanderthal tooth enamel

This example illustrates the possibility offered by the *DosiVox* software to use 3D images for building the geometry. Indeed, dose attenuation is not the only factor necessary for calculating the dose rate to which the enamel is exposed: the tooth shape and the distribution of the radioelements in the dentin and ivory are often complex and affect the  $\beta$ -dose rate determination; they undoubtedly must be taken into account. A tooth model was built using a 3D image obtained from a micro-scanner tomography of a left maxillary deciduous molar associated to the Roc de Marsal Neanderthal child skull (Bayle et al., 2009). A 3D visualization of the model with the 3D viewer *ImageJ* plugin (available at the *ImageJ* website) is presented in Fig. 11; this 3D image is available in the NESPOS data base (<https://www.nespos.org/display/openspace/Home>). A uranium distribution model has been created considering a fast uranium uptake in the most organic parts of the tooth from the burial sediment, followed by a progressive diffusion of this radioelement in the dentin (Fig. 12). Because of the disequilibrium in the U series, each value of the uranium content has to represent the content averaged over the burial time. This model of uranium uptake does not match any real data from the tooth nor any real model of radio-elements uptake: it was simply constructed by successive dilatations in the three dimensions of the 3D image of the dental pulp zone, restricted at each step by the ivory zone. These operations were made with the 3D *ImageJ* suite plugin (Ollion et al., 2013).

Both the models concerning the structure and the radioactive distribution have been used as input data for the voxelised detector, and the simulation parameters have been set to create a dose distribution mapping in the enamel. Simulations of both the clay burial sediment dose and the internal dose have been performed. The resulting dose mapping can

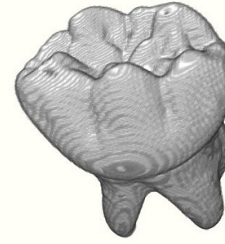


Figure 11. 3D view of the Neanderthal tooth model (*ImageJ*, 3D viewer plugin)

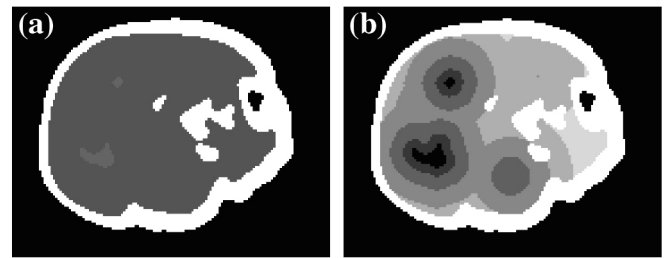


Figure 12. Slices of the tooth material 3D map and its radioactive content map: (a) material map, (b) radioactive content map (arbitrary scale, the darkest shades indicate the highest contents)

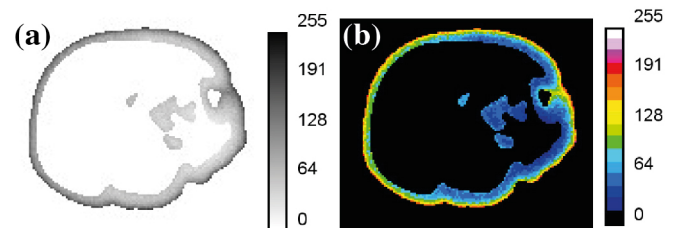


Figure 13.  $\beta$ -dose rate map in the tooth enamel (arbitrary scale): (a) dose distribution as a grey shades image, (b) dose distribution as a colour image

be read with the *ImageJ* software to reconstruct a 3D image of the dose distribution in the enamel. Figure 13 shows a slice of this image, corresponding to the Fig. 12 level. A heterogeneous dose distribution is observed in the enamel, as expected.

The results presented here are only intended to illustrate the possibility of calculating spatially resolved dose rates in a complex sample. In fact, there is no data for this precise sample about radioelements distribution, and no dating problematic about it either. In addition, the spectrum used for  $\beta$ -emission corresponds to the uranium series at equilibrium, which is obviously not common in a tooth because of the disequilibrium induced by the uptake of soluble elements of the series. But once again, the aim of this construction is not to discuss complex effects relating to uranium uptake but simply to illustrate the possibilities offered by *DosiVox*.

In the future, accurate data for both the tooth structure and

its radioactive contents, associated with a model of radioelement uptake during burial, should allow constructing reliable models in the same way as what was done in this example. Such a model would allow calculating the dose rates in every part of the tooth, for example, taking into account the disequilibrium in the U series.

### 3.5. $\beta$ -micro-dosimetry in a stratified sediment

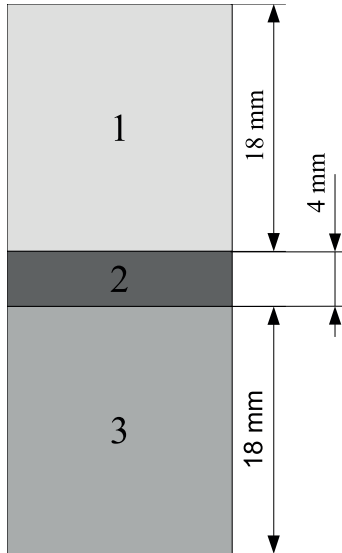


Figure 14. Plan of the geometry of the stratified sediment model: (1) clay, density =  $2 \text{ g/cm}^3$ , WF = 10 %,  $100 \mu\text{m}$  grains with a compacity of 5 %, Th content: 2 ppm, (2) sand, density =  $1.9 \text{ g/cm}^3$ , WF = 18 % 40 % volumic of  $200 \mu\text{m}$  grains, 45 % volumic of  $100 \mu\text{m}$  grains, 15 % volumic of  $50 \mu\text{m}$  grains with a total compacity of 60 %, Th content: 1 ppm, (3) clay with organic matter, density =  $1.8 \text{ g/cm}^3$ , WF = 15 %,  $100 \mu\text{m}$  grains with a compacity of 5 %, Th content: 3 ppm

This example deals with the dose rates to which individual quartz grains distributed in a sediment are exposed. In the case of heterogeneous or micro-stratified sediments, micro-dosimetric phenomena can occur. In order to assess the influence of these effects on the dose received by the grains, we used the graphical interface for constructing a sedimentary environment. The simple model considered here is composed of a thin level of sand surrounded by two clay deposits, one of them being rich in organic matter (Fig. 14). The clay contained quartz grains of  $100 \mu\text{m}$  in diameter, representing 5 % of the volume. The sand stratum is composed of  $200 \mu\text{m}$ ,  $100 \mu\text{m}$  and  $50 \mu\text{m}$  quartz grains, representing respectively 40 %, 45 % and 15 % of the volume of the grains. This volume accounts for 60 % of the sand level volume, and the remaining 40 % is filled with water (representing an average water content of about 18 % (in mass) for this stratum). In spite of the small thickness of this level compared to the clay levels (4 mm compared to 18 mm for the clay levels), about half of the  $100 \mu\text{m}$  grains defined in this model are included in the sand stratum. Each stratum contains a different content of thorium, which are 2 ppm, 1 ppm and 3 ppm, respectively,

for the clay stratum, the sand stratum and the stratum made of organic matter rich clay. *DosiVox* was used to calculate the  $\beta$ -dose distribution from the thorium series (at secular equilibrium) to the  $100 \mu\text{m}$  grains, regardless of their location in the three defined levels. These doses were normalized with the medium dose received by the  $100 \mu\text{m}$  grains localized in the part of the model non-affected by edge effects (i.e. for z values ranging from 5 mm to 35 mm). The micro-dosimetric impact of this configuration can be observed in Fig. 15, confirming that such scenarios can generate significant scatter in  $\beta$ -dose and dose distributions. The dose is distributed between three peaks corresponding to each level of the sediment and partially recovering themselves. The lower doses (centered around 0.6 of the average dose value), corresponding to grains localized in the sandy level, shows a Gaussian profile stretched in the direction of the higher doses. This shape results from grains located near the boundaries between the sand stratum and the more radioactive levels of clay.

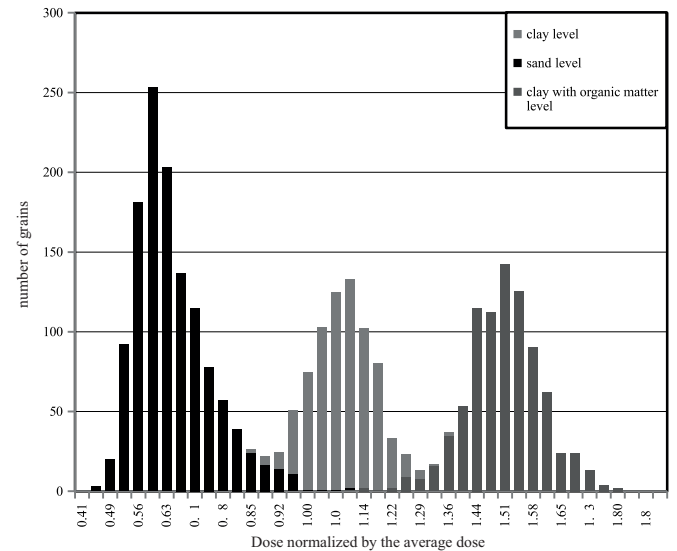


Figure 15. Dose distribution in the  $100 \mu\text{m}$  grains. The tints indicate the stratum of origin of the grains

It is also interesting to notice that, in considering the average  $\beta$ -dose and the water content of the present model, it is possible to calculate the dose one could determine in performing, for instance,  $\gamma$ -ray spectrometry measurements on a bulk sediment (resulting from the mixing of the three levels). The calculation shows that this dose would correspond to a value of 1.3 of the average simulated dose received by all the  $100 \mu\text{m}$  quartz grains.

### 3.6. Bursts of $\beta$ - and $\alpha$ -particles

The interactions of ionizing particles in matter depend largely on the particles nature, their energy and the matter properties in which they pass through. Studying these interactions can be useful for understanding many dosimetric effects. With *DosiVox*, it is easy to model a burst of particles and to record the dose deposited in a particular material. This

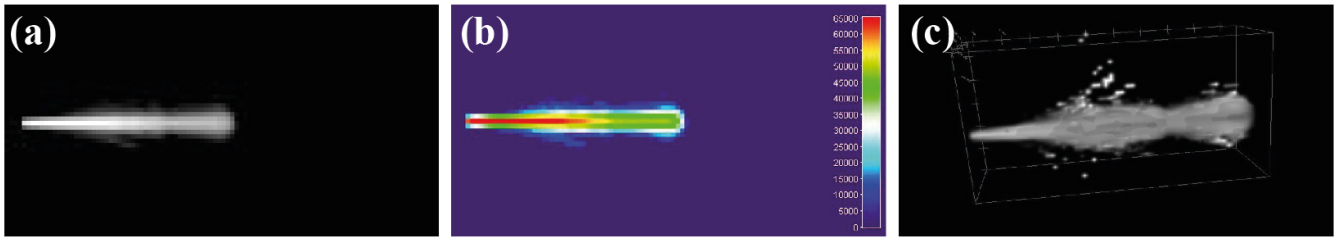


Figure 16. Dose deposition map for an  $\alpha$ -particles spray with the energetic spectrum of the thorium series

model has been constructed with the *ImageJ* software and is based on a cubical 3D image made of  $100 \times 100 \times 100$  voxels, containing a single grey tinted voxel defining the emission point. This image, saved as an ASCII text image sequence, has been first loaded in *DosiVox* to define the voxelised detector and secondly, filled with a clay type material (chemical composition in mass:  $\text{SiO}_2$  55 %,  $\text{Al}_2\text{O}_3$  35 %,  $\text{Fe}_2\text{O}_3$  10 %; density:  $2 \text{ g/cm}^3$ , water content: 13 %). A unidirectional emission was chosen, and the dose deposited in the detector recorded as a 16 bits 3D image.

The central slices of the images obtained for the  $\beta$ - and  $\alpha$ -particles emitted by the thorium series are presented in Fig. 16 and Fig. 17, respectively. The visualization was made by importing the images in *ImageJ* as text images. In both of them, the grey values represent the dose deposited (using a logarithmic scale).

The dose distribution from  $\alpha$ -particles seems localized in two volumes: a first burst corresponds to  $\alpha$ -particles with energies between 3.8 MeV and 6.8 MeV, and a more distant zone results from the 8.8 MeV  $\alpha$ -emission of the thorium series.

Conversely, the  $\beta$ -dose distribution in the detector indicates very diffusive trajectories for the particles, as expected.

#### 4. Discussions

The examples presented above were not intended specifically to deliver definitive data, rather to illustrate some of the numerous possibilities of the *DosiVox* software for modeling complex dosimetric systems, and providing a tool for dose rate calculations. The statistical precision of the results presented depends on simulation times, but users should also be conscious of other factors which influence the accuracy of such models.

The first category concerns the input data: to create a precise model of a sample, data concerning the structure, the chemical composition and the radioelement contents at the concerned size level are required. Where approximations are needed in describing the materials they can limit the accuracy of the calculated doses.

Additionally consideration should be given to the program input constraints. Since the main purpose of *DosiVox* was to create a user friendly interface to a flexible series of granular configurations there are limits to the complexity of the geometries that can be defined. In particular, the interface

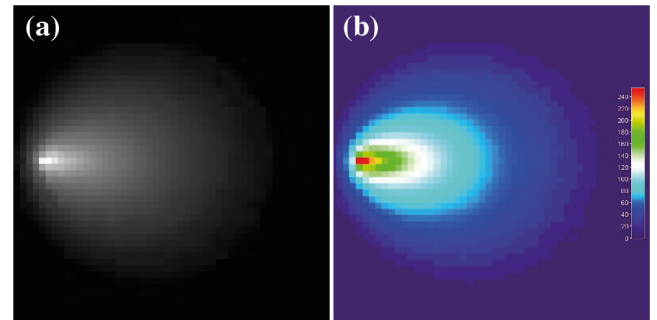


Figure 17. Dose deposition map for a  $\beta$ -particles spray with the energetic spectrum of the thorium series: (a) 8-bit slice of the dose deposition 3D map, (b) colored slice of the dose deposition 3D map (arbitrary logarithmic scale)

allows defining a grid with only 20 voxels in each direction. The user has then to choose wisely the dimensions of the geometry he wants to reproduce, considering the particle transport characteristics, the sample complexity, and possible edge effects, to ensure that the requested accuracy can be reached. Nevertheless, the user can define a higher resolution, as it was done in the last example, in loading in *DosiVox* 3D images.

Finally it is important to remember the limitations imposed by the models describing the physical interactions: the physics models available in *Geant4* do not perfectly reproduce the behavior of the particles, leaving small but non-zero errors induced by the modeling of the particle-matter interactions. An important parameter of the model is the secondary particle production cut-off, expressed as a range cut value and which can be chosen using the graphical interface or editing the pilot text file. This value is a limit in range for secondary particle production, below which these particles are not explicitly simulated by *Geant4*, but are replaced by a local energy deposition (this process allows avoiding any infrared divergence). Considering the range of the  $\alpha$ -particles and the very diffusive path of the  $\beta$ -particles in sediment, sub micron cut-off values are recommended for these radiations. Above this value, simulation runs are considerably faster but the dose deposited in volumes with dimensions lower than a millimeter can be significantly biased. If one wants to set a cut in range higher than the micrometer for  $\beta$ - and  $\alpha$ -particles, we recommend testing the simulation with a



smaller cut, to estimate the difference in the results.

Finally, one has to remember that the numbers manipulated by the processors of our computers often contain indeterminations related to conversions between the binary and decimal systems. These indeterminations can lead to small errors, which accumulate in particular when considering large sums of small numbers, as it can be the case for dose calculation.

## 5. Conclusions

The *DosiVox* software allows modeling numerous different configurations for which simulations are required for dosimetric calculations. For dating, when considering the appropriate data set and making reasonable hypotheses, it is possible to model a sample in its environment, to define the different materials and their radioactive contents and finally, to run simulations for calculating the dose rate to which it is exposed.

The graphical interface and the possibility of editing the pilot text file allow non-programmer users to easily create their own models and run their simulations. However, a minimal investment about the functioning of both the interface and the program remains necessary, considering the variety of parameters that have to be defined. Skills about image processing can be considerable, as much for creating complex geometrical models for inputting in the voxelised detector as well as for processing the images representing the deposited dose.

With actual computers, statistically accurate simulations require few hours to several days, but it is still possible to run several parallel simulations in the limits of the computing resources at hand (for instance in using several processing cores) and to compile the results of each of them. Clusters or multi-core computers are useful tools for this task as well.

*DosiVox* can then be freely downloaded at the following address: <http://www.iram-at-crp2a.cnrs.fr/spip/spip.php?article144>.

## Acknowledgments

The authors are grateful to H el ene Coqueugniot and Priscilla Bayle from the PACEA laboratory (Bordeaux, France) who provided the micro-scanner tomography images. We also thank Makoto Asai from SLAC (Stanford University, CA, USA) for his help concerning geometry navigation and optimization in *Geant4*, and Mathieu Karamitros from CENBG (Gradignan, France) for useful advice in programming. This work has been supported by the LaS-cArBx (Labex Sciences Arch eologiques de Bordeaux) ANR-10-LABX-52 and by the Conseil R egional d'Aquitaine DOSI-ART project.

## References

- Ab ramoff, M.D., Magalh aes, P.J., and Ram, S.J. *Image Processing with ImageJ*. Biophotonics International, 11(7): 36–42, 2004.
- Agostinelli, S., Allison, J., Amako, K., Apostolakis, J., Araujo, H., Arce, P., Asai, M., Axen, D., Banerjee, S., Barrand, G., Behner, F., Bellagamba, L., Boudreau, J., Broglia, L., Brunengo, A., Burkhardt, H., Chauvie, S., Chuma, J., Chytracek, R., Cooperman, G., Cosmo, G., Degtyarenko, P., Dell'Acqua, A., Depaola, G., Dietrich, D., Enami, R., Feliciello, A., Ferguson, C., Fesefeldt, H., Folger, G., Foppiano, F., Forti, A., Garelli, S., Giani, S., Giannitrapani, R., Gibin, D., Cadenas, J.J. G omez, Gonzlez, I., Abril, G. Gracia, Greeniaus, G., Greiner, W., Grichine, V., Grossheim, A., Guatelli, S., Gumplinger, P., Hamatsu, R., Hashimoto, K., Hasui, H., Heikkinen, A., Howard, A., Ivanchenko, V., Johnson, A., Jones, F.W., Kallenbach, J., Kanaya, N., Kawabata, M., Kawabata, Y., Kawaguti, M., Kellner, S., Kent, P., Kimura, A., Kodama, T., Kokoulin, R., Kossov, M., Kurashige, H., Lamanna, E., Lamp en, T., Lara, V., Lefebure, V., Lei, F., Liendl, M., Lockman, W., Longo, F., Magni, S., Maire, M., Medernach, E., Minamimoto, K., de Freitas, P. Mora, Morita, Y., Murakami, K., Nagamatu, M., Nartallo, R., Nieminen, P., Nishimura, T., Ohtsubo, K., Okamura, M., O'Neale, S., Oohata, Y., Paech, K., Perl, J., Pfeiffer, A., Pia, M.G., Ranjard, F., Rybin, A., Sadilov, S., Salvo, E. Di, Santin, G., Sasaki, T., Savvas, N., Sawada, Y., Scherer, S., Sei, S., Sirotenko, V., Smith, D., Starkov, N., Stoecker, H., Sulkimo, J., Takahata, M., Tanaka, S., Tcherniaev, E., Tehrani, E. Safai, Tropeano, M., Truscott, P., Uno, H., Urban, L., Urban, P., Verderi, M., Walkden, A., Wander, W., Weber, H., Wellisch, J.P., Wenaus, T., Williams, D.C., Wright, D., Yamada, T., Yoshida, H., and Zschiesche, D. *Geant4—a simulation toolkit*. Nuclear Instruments and Methods in Physics Research Section A: Accelerators, Spectrometers, Detectors and Associated Equipment, 506(3): 250–303, 2003.
- Aitken, M.J. *Thermoluminescence Dating*. Academic Press, London, 1985.
- Aitken, M.J., Clark, P.A., Gaffney, C.G., and L ovborg, L. *Beta and gamma gradients*. Nuclear Tracks and Radiation Measurements, 10(4-6): 647–653, 1985.
- Allison, J., Amako, K., Apostolakis, J., Araujo, H., Dubois, P.A., Asai, M., Barrand, G., Capra, R., Chauvie, S., Chytracek, R., Cirrone, G.A.P., Cooperman, G., Cosmo, G., Cuttone, G., Daquino, G.G., Donszelmann, M., Dressel, M., Folger, G., Foppiano, F., Generowicz, J., Grichine, V., Guatelli, S., Gumplinger, P., Heikkinen, A., Hrivnacova, I., Howard, A., Incerti, S., Ivanchenko, V., Johnson, T., Jones, F., Koi, T., Kokoulin, R., Kossov, M., Kurashige, H., Lara, V., Larsson, S., Lei, F., Link, O., Longo, F., Maire, M., Mantero, A., Mascialino, B., McLaren, I., Lorenzo, P.M., Minamimoto, K., Murakami, K., Nieminen, P., Pandola, L., Parlati, S., Peralta, L., Perl, J., Pfeiffer, A., Pia, M.G., Ribon, A., Rodrigues, P., Russo, G., Sadilov, S., Santin, G., Sasaki, T., Smith, D., Starkov, N., Tanaka, S., Tcherniaev, E., Tome, B., Trindade, A., Truscott, P., Urban, L., Verderi, M., Walkden, A., Wellisch, J.P., Williams, D.C., Wright, D., and Yoshida, H. *Geant4 developments and applications*. Nuclear Science, IEEE Transactions on, 53(1): 270–278, Feb 2006.
- Aso, T., Kimura, A., Yamashita, T., and Sasaki, T. *Optimization of patient geometry based on CT data in GEANT4 for medical application*. Nuclear Science Symposium Conference Record, 2007.NSS '07. IEEE, Volume 4, 2007.

- Baró, J., Sempau, J., J.M.Fernández-Varea, and Salvat, M. *PENELOPE: an algorithm for Monte Carlo simulation of the penetration and energy loss of electrons and positrons in matter*. Nuclear Instruments Methods in Physics Research B, 100: 31–46, 1995.
- Bayle, Priscilla, Braga, José, Mazurier, Arnaud, and Macchiarelli, Roberto. *Dental developmental pattern of the Neanderthal child from Roc de Marsal: a high-resolution 3D analysis*. Journal of human evolution, 56(1): 66–75, January 2009.
- Bell, W.T. *Alpha dose attenuation in quartz grain for thermoluminescence dating*. Ancient TL, 12: 4–8, 1980.
- Fleming, S.J. *Thermoluminescence dating : refinement of the quartz inclusion method*. Archaeometry, 12: 133–147, 1970.
- Guérin, G., Mercier, N., Nathan, R., Adamiec, G., and Lefrais, Y. *On the use of the infinite matrix assumption and associated concepts: a critical review*. Radiation Measurements. Radiation Measurements, 47: 778–785, 2012.
- Incerti, S., Seznec, H., Simon, M., Barberet, Ph., Habchi, C., and Moretto, Ph. *Monte Carlo dosimetry for targeted irradiation of individual cells using a microbeam facility*. Radiation Protection Dosimetry, 133: 2–11, 2009.
- Ivanchenko, V., Apostolakis, J., Bagulya, A., Abdelouahed, H.B., Black, R., Bogdanov, A., Burkhard, H., Chauvie, S., Cirrone, P., Cuttone, G., Depaola, G., Di Rosa, F., Elles, S., Francis, Z., Grichine, V., Gumplinger, P., Gueye, P., Incerti, S., Ivanchenko, A., Jacquemier, J., Lechner, A., Longo, F., Kadr, O., Karakatsanis, N., Karamitros, M., Kokoulin, R., Kurashige, H., Maire, M., Mantero, A., Mascialino, B., Moscicki, J., Pandola, L., Perl, J., Petrovic, I., Ristic-Fira, A., Romano, F., Russo, G., Santin, G., Schaelicke, A., Toshito, T., Tran, H., Urban, L., Yamashit, T., and Zacharatou, C. *Recent improvements in Geant4 electromagnetic physics models and interfaces*. Progress in Nuclear. Science and Technology, 2: 898–903, 2011.
- Mejdahl, V. *Thermoluminescence dating: beta-dose attenuation in quartz grains*. Archaeometry, 21: 61–73, 1979.
- Ollion, Jean, Cochenec, Julien, Loll, François, Escudé, Christophe, and Boudier, Thomas. *TANGO: a generic tool for high-throughput 3D image analysis for studying nuclear organization*. Bioinformatics (Oxford, England), 29(14): 1840–1841, July 2013.
- Rasband, W.S. *ImageJ, U.S. National Institutes of Health, Bethesda, Maryland, USA, 1997–2012*. [imagej.nih.gov/ij/](http://imagej.nih.gov/ij/).
- Schneider, C.A., Rasband, W.S., and Eliceiri, K.W. *NIH Image to ImageJ: 25 years of image analysis*. Nature Methods, 671: doi:10.1038/nmeth.2089, 2012.
- Sempau, J., Fernández-Varea, J.M., Acosta, E., and Salvat, F. *Experimental benchmarks of the Monte Carlo code PENELOPE*. Nuclear Instruments and Methods in Physics Research B, 207: 107–123, 2003.
- Zimmerman, D.W. *Thermoluminescent dating using fine grains from pottery*. Archaeometry, 10: 26–28, 1971.

## Reviewer

David Sanderson